Image-guided WEMVA for azimuthal anisotropy

Yunyue (Elita) Li

SUMMARY

Azimuthal anisotropy is common in layered basins with strong folding and fracturing effects. Traditional processing on individual azimuths usually yields images with inconsistent depths. In this paper, we propose to use an image obtained from one azimuth to constrain the image-space velocity analysis on other azimuths. This method directly tackles the differences in anisotropic parameters among different azimuths. By keeping the vertical velocity constant across the azimuths, we separate the kinematic effects due to the anisotropic parameters from those due to the velocity error. We test the image-guided migration velocity analysis algorithm on a 2-D example with flat reflectors and a homogeneous orthorhombic subsurface. We compare the residual images and the first η gradient obtained by our image-guided method with the differential semblance method under three different conditions: accurate velocity, fast velocity and slow velocity. Our results show that despite the velocity error, the image-guided migration velocity analysis algorithm provides consistent η gradients, whereas the gradients given by differential semblance optimization may be misled by the velocity error.

INTRODUCTION

Since it was first reported in exploration seismology in the 1930s (McCollum and Snell, 1932), anisotropy has played an increasingly important role in seismic imaging and exploration. Until now, the layered transverse isotropic (TI) model has been the most commonly used model in seismic imaging. Due to changes in the surrounding stress fields, small scale fractures or cracks may form in the layered media. The combination of parallel vertical cracks and vertical transverse anisotropy in the background medium is the most common cause of an effective orthorhombic medium (Figure 1). Efficient and accurate wave propagation in the orthorhombic medium has been extensively studied (Tsvankin, 1997; Cheng et al., 2012), with new developments in wave-equation based orthorhombic propagation in recent years (Zhang and Zhang, 2011; Fowler and Lapilli, 2012; Chu, 2012). These developments help the understanding of the wave phenomenon in complex geological settings. However, reliable inversion for the elastic parameters needed for orthorhombic modeling is still under investigation.

To fully describe an orthorhombic medium, one must constrain the nine independent parameters in the elastic tensor. Early methods based on shear wave splitting are useful to detect the orientation of the fractures (Garotta, 1989; Olofsson et al., 2003); however, they are far from sufficient to constrain the whole medium. Tsvankin (1997) reparameterizes the orthorhombic medium and reduces the number of parameters to six governing P-wave propagation in the orthorhombic medium. This reduction of the parameter and analysis on the P-wave propagation in the symmetrical planes shed light on the parameter estimation: to fully constrain all six parameters, we need data from six different azimuths. With the modern full azimuthal acquisition, especially OBS and coil shooting acquisition, this requirement is not difficult to meet.

Now the question remains: given full azimuth data, how should we process the data and build a corresponding orthorhombic model? Recent studies analyze the non-hyperbolic normal moveout of the data to invert for the orthorhombic parameters (Grechka and Tsvankin, 1999; Elapavuluri and Bancroft, 2006; Vasconcelos and Tsvankin, 2006). However, these data space methods are prone to noise in the data and may require over-simplification of the subsurface structures.

This study discusses one possible way to directly resolve the velocity differences among different azimuths in the image space. We propose to work with one azimuth at a time. Once the first 3-D image from the first azimuth is properly obtained, we can use this image as a reference to constrain the inversion at the other azimuths. The idea of defining a penalty function according to an existing image is not new, but was first proposed by Shragge and Lumley (2013) to highlight time-lapse velocity changes in the subsurface. We borrow the same idea and apply it to resolve the differences among different azimuths, and hence to resolve the azimuthal anisotropy.

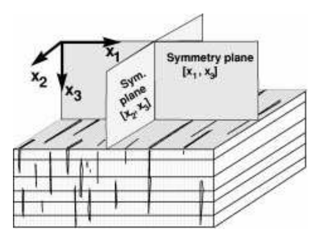

Figure 1: An orthorhombic model caused by parallel vertical cracks embedded in a VTI medium. Orthorhombic media have three mutually orthogonal planes of mirror symmetry. From Tsvankin (1997).

ANISOTROPIC PARAMETERS FOR P-WAVE PROPAGATION IN ORTHORHOMBIC MEDIUM

Following a definition similar to Thomsen's (Thomsen, 1986), Tsvankin (1997) parameterized orthorhombic media using similar velocity and dimensionless coefficients as follows:

- V_{P0} – the vertical velocity of the P-wave;
- V_{S0} – the vertical velocity of the S-wave polarized in the x_1 direction;
- $\varepsilon^{(2)}$ – the VTI parameter ε in the symmetry plane $[x_1, x_3]$;
- $\delta^{(2)}$ – the VTI parameter δ in the symmetry plane $[x_1, x_3]$;
- $\gamma^{(2)}$ – the VTI parameter γ in the symmetry plane $[x_1, x_3]$;

DOI http://dx.doi.org/10.1190/segam2013-0449.1

- $\varepsilon^{(1)}$ – the VTI parameter ε in the symmetry plane $[x_2, x_3]$;
- $\delta^{(1)}$ – the VTI parameter δ in the symmetry plane $[x_2, x_3]$;
- $\gamma^{(1)}$ – the VTI parameter γ in the symmetry plane $[x_2, x_3]$;
- $\delta^{(3)}$ – the VTI parameter δ in the symmetry plane $[x_1, x_2]$.

Under the assumption of weak anisotropy, the phase velocity of the P-wave is as follows:

$$V_p(\theta,\phi) = V_p0[1+\delta(\phi)\sin^2\theta\cos^2\theta+\varepsilon(\phi)\sin^4\theta]; \quad (1)$$

with azimuthal dependent anisotropic parameters $\varepsilon(\phi)$ and $\delta(\phi)$ defined by

$$\varepsilon(\phi) = \varepsilon^{(1)}\sin^4\phi+\varepsilon^{(2)}\cos^4\phi+(2\varepsilon^{(2)}+\delta^{(3)})\sin^2\phi\cos^2\phi, \quad (2)$$

$$\delta(\phi) = \delta^{(1)}\sin^2\phi+\delta^{(2)}\cos^2\phi. \quad (3)$$

It can be seen from equation 1 through 3 that kinematic signatures of P-wave in weak orthorhombic media depend on just *five* anisotropic parameters in the symmetric planes and the vertical P-wave velocity. This reduction of parameters gives us hope to resolve a reliable orthorhombic model using modern full azimuth acquisition geometry.

IMAGE-GUIDED WEMVA

Although 3-D seismic acquisition and processing has been performed in practice for more than two decades (Biondi, 2006), conventional processing workflows still work with narrow azimuth data and process a single azimuth at a time. One of the key aspects of image-space WEMVA is the definition of the "target" image (Biondi, 2006), which subsequently defines the residual image used for gradient computation. The WEMVA objective function in the subsurface offset domain can be written as follows:

$$J = ||\mathbf{W}(\mathbf{h})\mathbf{I}(\mathbf{x},\mathbf{h})||_2^2. \quad (4)$$

Differential semblance optimization (DSO) (Shen and Symes, 2008) has been a popular choice for defining the "target" image thanks to its simplicity in concept and automation in implementation. Equation 5 shows the weighting function defined by the conventional DSO objective function, where h is the length of the subsurface offset $\mathbf{h}$ and h_{max} is the maximum subsurface offset.

$$\mathbf{W}_{\text{dso}}(\mathbf{x},\mathbf{h}) = \frac{h}{h_{max}}. \quad (5)$$

Hence, the DSO objective function leads to a residual image as follows:

$$\Delta\mathbf{I}_{\text{dso}} = \mathbf{W}^*_{\text{dso}}\mathbf{W}_{\text{dso}}\mathbf{I}(\mathbf{x},\mathbf{h}), \quad (6)$$

where $\mathbf{I}$ is the common image gathers in the subsurface offset domain. Notice that the DSO weighting function is invariant with the spatial coordinates.

On the other hand, many authors (Fei and Williamson, 2010; Vyas and Tang, 2010) have pointed out various artifacts in the DSO gradient, such as side lobes and scattering effects. Therefore, we need a better way to define the residual image and the objective function. In modern acquisition, where the subsurface is illuminated from all angles (up to the angle defined by the maximum offset) and full azimuths, we can obtain up to a seven-dimension image cube of the subsurface. Due to this redundancy, it is possible to form not only image gathers with respect to reflection angle, but also the multi-azimuth image gathers. Although full 3D imaging technique has existed for more than two decades, single azimuthal processing is still the common practice in the industry. Therefore, the image obtained from one azimuth can be used as the "target" image for the other azimuths.

Here, we propose to define the weighting function according to the envelope of the existing image:

$$\mathbf{W}_{\text{img}}(\mathbf{x},\mathbf{h}) = 1 - \frac{E(\mathbf{I_0}(\mathbf{x},\mathbf{h}))}{\max(E(\mathbf{I_0}(\mathbf{x},\mathbf{h})))}, \quad (7)$$

where E denotes the envelope function and $\mathbf{I_0}$ is the reference image at a certain azimuth.

To test our velocity analysis method by matching images at two different azimuths, we take advantage of the fact that the P-wave propagation is fully described using conventional VTI wave equations in the symmetric planes. The only difference is that the "VTI parameters" are different in each plane. Nonetheless, they do share the same vertical P-wave velocity.

NUMERICAL TEST

In this section, we test our idea on a simple numerical model. The synthetic model contains five flat reflectors, and the velocity and anisotropic parameters are constant. We take advantage of the fact that the P-wave propagation is fully described using conventional VTI wave equations in the symmetric planes, and we model the data at azimuth 0° and azimuth 90° using the same VTI one-way wave-equation with different values for the parameters: at azimuth 0°, $V_{P0} = 2000 m/s$, $\eta^{(2)} = 0.2$, $\delta^{(2)} = 0.1$; at azimuth 90°, $V_{P0} = 2000 m/s$, $\eta^{(1)} = 0.4$, $\delta^{(1)} = 0.1$.

We first migrate both datasets at azimuth 0° and 90° using the same migration model: $V_{P0} = 2000 m/s$, $\eta = 0.2$, $\delta = 0.1$. In this case, the subsurface model is exact for azimuth 0°. Therefore, in the subsurface-offset common image gathers (CIGs) at azimuth 0° on panel (a) in figure 2, the events are almost focused at the zero subsurface-offset, except for some illumination artifacts at the deeper reflectors. However, the downward curvature on panel (b) in figure 2 is due to the negative error in the η model. Thanks to the wider angle coverage, the kinematic differences between two azimuthal images are more significant on the shallower reflectors than on the deeper ones.

To penalize the unfocused image at azimuth 90°, the DSO weighting matrix $\mathbf{W}_{\text{dso}}$ can be applied at each image point in the subsurface offset domain, as shown in panel (a) of in figure 8. Notice that the weighting function is uniformly distributed vertically, regardless of the illumination effects. Also, the DSO penalty function is independent of the vertical velocity error. On the other hand, we can also design the penalty function according to the image at azimuth 0° using equation 7. The image-guided penalty function $\mathbf{W}_{\text{img}}$ with the exact vertical velocity is shown in panel (b) in figure 8.

DOI http://dx.doi.org/10.1190/segam2013-0449.1

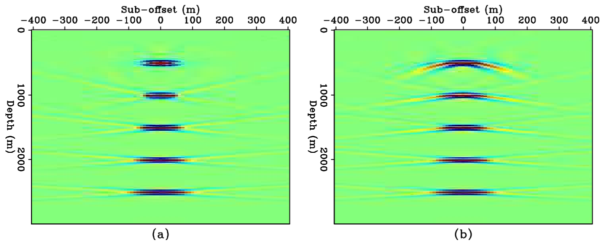

Figure 2: Subsurface-offset gathers at $x = 0m$ at azimuth 0° (a) and azimuth 90° (b). Migration parameters used in both data are $V_{P0} = 2000$ m/s, $\eta = 0.2$, $\delta = 0.1$.

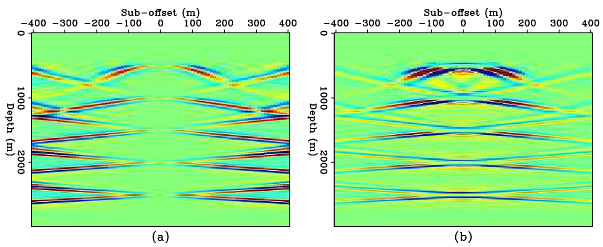

Figure 3: Residual subsurface-offset image at azimuth 90° using DSO penalty function (a) and image-guided penalty function (b). Migration parameters are $V_{P0} = 2000$ m/s, $\eta = 0.2$, $\delta = 0.1$.

The residual images produced by DSO and the image-guided penalty function are shown in panels (a) and (b) in figure 3, respectively. Notice that the DSO penalty function highlights the leaked energy from the zero subsurface offset, whereas the image-guided penalty function highlights the kinematics differences between two azimuths. When the vertical velocity model is exact, the leaked energy and the kinematics differences are both caused by the error in the η model only.

Back-projections of the residual images define the gradient direction in the model space. We stack the gradient over the horizontal axis, since the error in the η model is homogeneous. The gradients in η produced by DSO and image-guided penalty functions are plotted in panels (a) and (d) in figure 9, respectively. Both gradients point to the correct update directions to compensate for the η error and show higher sensitivity to the shallower reflectors than the deeper reflectors.

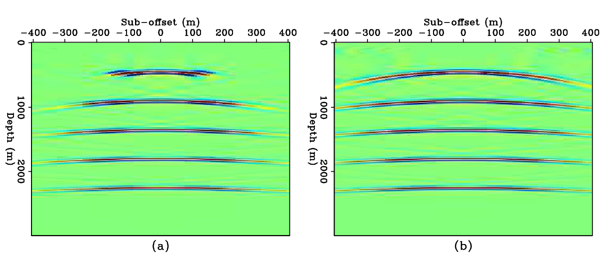

Figure 4: Subsurface-offset gathers at $x = 0m$ at azimuth 0° (a) and azimuth 90° (b).Migration parameters used in both data are $V_{P0} = 1800$ m/s, $\eta = 0.2$, $\delta = 0.1$.

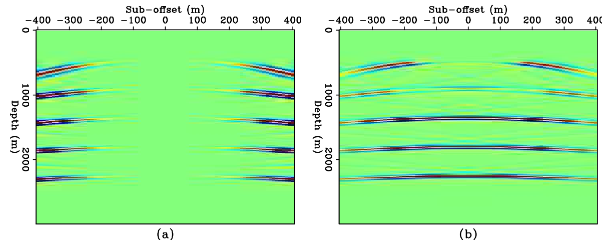

Figure 5: Residual subsurface-offset image at azimuth 90° using DSO penalty function (a) and image-guided penalty function (b). Migration parameters are $V_{P0} = 1800$ m/s, $\eta = 0.2$, $\delta = 0.1$.

To test the ambiguity between velocity and η, we assume the vertical velocity is not accurately estimated. The parameters used in the second test are: $V_{P0} = 1800$ m/s, $\eta = 0.2$, $\delta = 0.1$. Notice that the error in vertical velocity is in the same direction as that in the η model for azimuth 90°. The background images at azimuths 0° and 90° are shown in figure 4. The downward curvature in panel (a) is caused by the negative vertical velocity error, while the broader curvature in panel (b) is caused by the additional negative error in η. Comparing the two images and ignoring the illumination effect, the only difference between the two images is caused by the η error.

Using the unfocused image at azimuth 0° as guidance, the highlighted differences between two azimuths are shown in figure 5(b). On the other hand, the residual image defined by DSO penalty function in 5 (a) includes the kinematic errors caused by both velocity and η error.

Back-projections of the residual images in figure 5 are plotted in panels (b) and (e) in figure 9. Both DSO and image-guided penalty functions point to the correct update direction. The updates of η is significantly stronger from the first reflector than from the deeper ones.

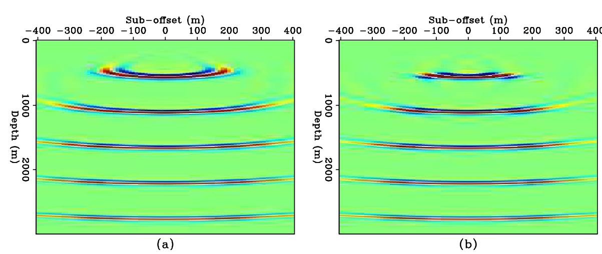

Figure 6: Subsurface-offset gathers at $x = 0m$ at azimuth 0° (a) and azimuth 90° (b). Migration parameters used in both data are $V_{P0} = 2200$ m/s, $\eta = 0.2$, $\delta = 0.1$.

A more interesting test of the ambiguity between velocity and η is to perturb the velocity model in the opposite direction to the η perturbation. Therefore, we migrate both datasets at both azimuths using $V_{P0} = 2200$ m/s, $\eta = 0.2$, $\delta = 0.1$. For azimuth 0°, the upward moveout in the background subsurface domain common image gathers (Figure 6(a)) is caused by the positive velocity error. For azimuth 90°, the narrower upward moveout is due to the trade-off effect between a positive velocity error

DOI http://dx.doi.org/10.1190/segam2013-0449.1

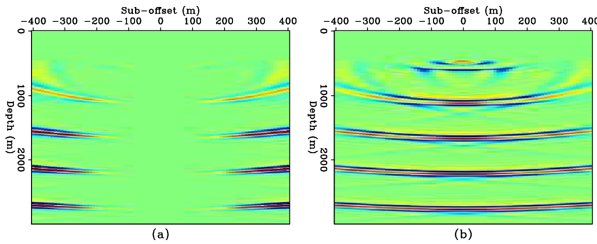

Figure 7: Residual subsurface-offset image at azimuth 90° using DSO penalty function (a) and image-guided penalty function (b). Migration parameters are $V_{P0} = 2200$ m/s, $\eta = 0.2$, $\delta = 0.1$.

and a negative velocity error. Since velocity has a first order effect on the kinematics of the wavefield, the overall characteristics in the subsurface offset domain at azimuth 90° indicate positive errors in the subsurface model.

The residual images produced by DSO and the image-guided penalty function are shown in figure 7, back-projections of which are plotted in panels (c) and (f) in figure 9, respectively. Clearly, due to the dominant effect of faster velocity, the DSO penalty function suggests to reduce the value of η, which kinematically reduces the velocity at large angles. However, the image-guided penalty function highlights the true kinematic error caused by η and successfully keeps the η update in the correct direction. This result shows that by using the image-guided penalty function, we have a chance to resolve the ambiguity between the velocity model and the η model.

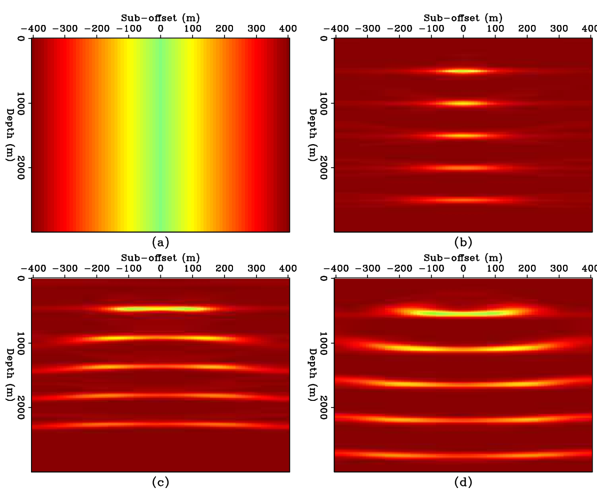

Figure 8: Spatial weighting function in the subsurface-offset domain at $x = 0$ m from DSO (a). Image-guided penalty function when the migration vertical velocity is the same (b), smaller (b) and larger (c) than the true vertical velocity.

CONCLUSIONS AND DISCUSSIONS

In this paper, we propose an image-guided penalty function to target the difference in anisotropic parameters at different

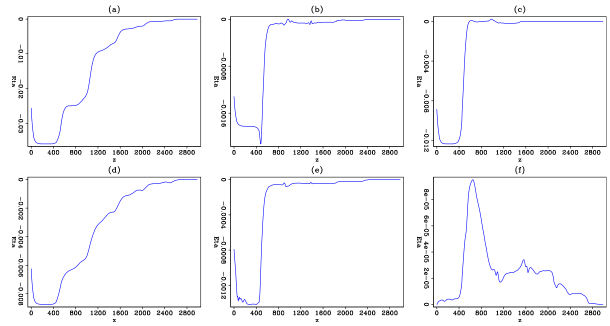

Figure 9: First gradient given by the image-guided penalty function (top row) and the DSO penalty function (bottom row). The columns from left to right correspond to the cases where the background velocity is the same, smaller or bigger than the true velocity, respectively.

azimuths. In an orthorhombic medium, the P-wave kinematics are governed by six parameters, among which the vertical velocity is shared by both azimuths in the $[x_1, x_3]$ plane and the $[x_2, x_3]$ plane. By fixing the migration models for both azimuths, and comparing the resulting images, we directly resolve the difference in the equivalent Thomsen parameters between both azimuths, regardless of the accuracy of the velocity model.

More importantly, the image-guided penalty function distinguishes the kinematic contribution of velocity from that of η by referencing the azimuthal images with the same velocity effects. The resulting residual image contains the only residual kinematics due to the difference in the anisotropic parameters. Therefore, regardless of the dominant effect of velocity error, the image-guided penalty function can produce correct updates for the anisotropic parameters.

However, the application of this method could potentially be limited by the subsurface structures and the acquisition geometry. For example, in areas with highly dipping reflectors and 3 D structures, the surface azimuths may no longer properly represent the azimuths in the subsurface. In this case, the subsurface azimuthal analysis may be used to evaluate the accuracy of the migration models. In addition, when acquisition geometries are significantly different across azimuths, the illumination differences may overwhelm the differences between the anisotropic parameters.

ACKNOWLEDGMENT

The authors acknowledge the sponsors of Stanford Exploration Project for their financial support.

DOI http://dx.doi.org/10.1190/segam2013-0449.1

http://dx.doi.org/10.1190/segam2013-0449.1

EDITED REFERENCES

Note: This reference list is a copy-edited version of the reference list submitted by the author. Reference lists for the 2013 SEG Technical Program Expanded Abstracts have been copy edited so that references provided with the online metadata for each paper will achieve a high degree of linking to cited sources that appear on the Web.

REFERENCES

Biondi, B., 2006, 3D seismic imaging: Investigations in Geophysics No. 14: SEG.

Cheng, X., J. Tang, O. Zdraveva, C. Yarman, and J. Hobro, 2012, Ray-based prestack depth migration for orthorhombic media: 82nd Annual International Meeting, SEG, Expanded Abstracts, http://dx.doi.org/10.1190/segam2012-0721.1.

Chu, C., 2012, A hybrid grid finite difference method for acoustic wave propagation in tilted orthorhombic media: 82nd Annual International Meeting, SEG, Expanded Abstracts, http://dx.doi.org/10.1190/segam2012-0745.1.

Elapavuluri, P. and J. Bancroft, 2006, Estimation of anisotropy parameters in orthorhombic media: 76th Annual International Meeting, SEG, Expanded Abstracts, 164–168, http://dx.doi.org/10.1190/1.2369837.

Fei, W. and P. Williamson, 2010, On the gradient artifacts in migration velocity analysis based on differential semblance optimization: 80th Annual International Meeting, SEG, Expanded Abstracts, 4071–4076, http://dx.doi.org/10.1190/1.3513710.

Fowler, P. and C. Lapilli, 2012, Generalized pseudospectral methods for orthorhombic modeling and reverse time migration: 82nd Annual International Meeting, SEG, Expanded Abstracts, 1–5, http://dx.doi.org/10.1190/segam2012-0708.1.

Garotta, R., 1989, Detection of azimuthal anisotropy: 69th Annual International Meeting, SEG, Expanded Abstracts, 861–863, http://dx.doi.org/10.1190/1.1889795.

Grechka, V., and I. Tsvankin, 1999, 3-D moveout velocity analysis and parameter estimation for orthorhombic media: Geophysics, **64**, 820–837, http://dx.doi.org/10.1190/1.1444593.

McCollum, B., and F. Snell, 1932, Asymmetry of sound velocity in stratified formations: Physics, **2**, 174–185, http://dx.doi.org/10.1063/1.1745044 (Journal of Applied Physics).

Olofsson, B., T. Probert, J. Kommedal, and O. Barkved, 2003, Azimuthal anisotropy from the Valhall 4C 3D survey: The Leading Edge, **22**, 1228–1235, http://dx.doi.org/10.1190/1.1641375.

Shen, P., and W. W. Symes, 2008, Automatic velocity analysis via shot profile migration: Geophysics, **73**, no. 5, VE49–VE59, http://dx.doi.org/10.1190/1.2972021.

Shragge, J., and D. Lumley, 2013, Time-lapse wave-equation migration velocity analysis: Geophysics, **78**, no. 2, S69–S79, http://dx.doi.org/10.1190/geo2012-0182.1.

Thomsen, L., 1986, Weak elastic anisotropy: Geophysics, **51**, 1954–1966, http://dx.doi.org/10.1190/1.1442051.

Tsvankin, I., 1997, Anisotropic parameters and P-wave velocity for orthorhombic media: Geophysics, **62**, 1292–1309, http://dx.doi.org/10.1190/1.1444231.

Vasconcelos, I., and I. Tsvankin, 2006, Non-hyperbolic moveout inversion of wide-azimuth P-wave data for orthorhombic media: Geophysical Prospecting, **54**, 535–552, http://dx.doi.org/10.1111/j.1365-2478.2006.00559.x.

Vyas, M. and Y. Tang, 2010, Gradients for wave-equation migration velocity analysis: 80th Annual International Meeting, SEG, Expanded Abstracts, 4077–4081, http://dx.doi.org/10.1190/1.3513711.

Zhang, H. J. and Y. Zhang, 2011, Reverse time migration in vertical and tilted orthorhombic media: 81st Annual International Meeting, SEG, Expanded Abstracts, 185–189, http://dx.doi.org/10.1190/1.3627568.

DOI http://dx.doi.org/10.1190/segam2013-0449.1